Università degli Studi di Padova

Padua Research Archive - Institutional Repository

Studies of silicon photomultipliers at cryogenic temperatures

(Article begins on next page)

Studies of silicon photomultipliers at cryogenic temperatures

G. Collazuol [a,*], M.G. Bisogni [a,b], S. Marcatili [a,b], C. Piemonte [c], A. Del Guerra [a,b]

[a] INFN Sezione di Pisa, 56127 Pisa, Italy
[b] Dipartimento di Fisica, Università di Pisa, 56127 Pisa, Italy
[c] Fondazione Bruno Kessler - IRST, Divisione Microsistemi, 38050 Trento, Italy

ARTICLE INFO

ABSTRACT

We investigate the behavior of silicon photomultipliers (SiPMs) at low temperatures: I–V characteristics, breakdown voltage, dark noise, afterpulsing, crosstalk, pulse shape, gain and photon detection efficiency are studied as a function of temperature in the range $50\,K < T < 320\,K$. We discuss our measurements on the basis of the temperature dependent properties of silicon and of the models related to carrier generation, transport and multiplication in high electric field. We conclude that SiPMs provide an excellent alternative to vacuum tube photomultipliers (PMTs) in low temperature environments, even better than in room temperature ones: in particular they excel in the interval $100\,K < T < 200\,K$.

1. Introduction

Recent technological improvements made SiPMs attractive alternative sensors for many detectors that would employ typically PMTs, in particular for applications at room temperature (T_{room}) where multi-photon detection is involved. Actually, state of the art sensitivity in light detection can be reached by operating SiPMs at low temperature. There, a whole range of potential applications is opened, from particle detection with noble liquids, to Cherenkov light detection where the small photon yield, opposed to the huge dark noise of SiPM at T_{room} makes cooling mandatory. In this work we report our studies about the behavior of SiPM at low temperature.

2. Experimental setup

We studied $1 \times 1\,mm^2$ FBK-IRST devices [1] of type T6-V1-PD (RunII-2006) with 625 square cells ($40 \times 40\,\mu m^2$), fill factor of $\sim 20\%$ and breakdown voltage of $\sim 33\,V$ at T_{room}. Each cell consists of an asymmetric shallow (100 nm) junction n^+–p implanted in a thin ($\sim 4\,\mu m$) lowly doped p-type epitaxial layer. The structure is grown on a low-resistivity p^+-type substrate. The micro-cells are connected in parallel via integrated poly-silicon quenching resistor ($R_q \sim 0.48\,M\Omega$ at T_{room}) and a common metal grid on one side and by the substrate on the other.

The anti-reflective coating on top of the silicon oxide layer is tuned for maximizing wavelengths around 450 nm. The samples are not covered with any protective epoxy layer.

The SiPM sample under study is cooled using a closed-cycle He cryocooler[1] in a vacuum vessel maintained at $P < 2 \times 10^{-3}$ mbar. Good thermal contact between the sample and the cryocooler head is ensured by inserting tightly the SiPM metallic socket into a hole on a copper rod which is fixed to the cryocooler head. The socket is electrically insulated from the rod by a thin sheet of Kapton. The sample temperature (T) is controlled by means of a heater ($1\,\Omega$) and stabilized using a PID controller for setting the heater current. The temperatures of SiPM, copper rod and cryocooler head are monitored by three platinum resistance thermometers[2] (Pt100). Each measurement is carried out after waiting for thermalization, when the temperature readout by the three probes coincide.

A halogen lamp coupled to a monochromator (wavelength range $200\,nm < \lambda < 900\,nm$) is employed for transmitting continuous light (CW) on to the surface of the SiPM via 0.5 mm quartz fibers entering the vacuum vessel. Fibers transport monochromatic light also to a calibrated photodiode[3] located outside the vessel, which is used for normalization. A UV-LED[4] ($\lambda = 380\,nm$) can be exploited for illuminating directly the sample

---

* Corresponding author.
E-mail address: gianmaria.collazuol@pi.infn.it (G. Collazuol).

[1] Helix model Cryodyne M-22, two stage refrigerator based on the Gifford–McMahon thermodynamic cycle.
[2] Specifically calibrated with dry ice (200 K) and LN$_2$ (77 K).
[3] Newport silicon photodiode model 918-UV.
[4] Toyoda UV-LED, gaussian spectrum width $\sim 25\,nm$ FWHM.

inside the vessel. Measurements are carried out also in pulsed mode with a laser[5] ($\lambda = 405$ nm) illuminating the fibers instead of the halogen lamp. Neutral filters allow for properly tuning the light intensity.

The SiPM is biased with a current–voltage source-meter[6] which we use for analog measurements. A ballast resistor ($R_b = 12.05 \pm 0.05$ kΩ) in series with the SiPM (cathode side) limits the current to prevent damages to the device. The SiPM substrate (anode) is capacitively coupled to a voltage amplifier[7] and is grounded through the amplifier input resistance ($R_{in} = 50\,\Omega$). The amplifier is located inside the vessel in order to minimize the cable length and it is thermally shielded from the cool head. The amplifier output signal is routed outside the vessel and readout by a sampling oscilloscope.[8] The vacuum vessel represents the common voltage reference (ground). In order to minimize the electromagnetic noise any lead, included the feedthroughs for signal and power supplies, is carefully shielded.

Measurements were performed in the temperature range $50\,\text{K} < T < 320\,\text{K}$. The SiPM samples have survived many vacuum pumping and thermal cycles showing very stable behavior. After short ($\sim \frac{1}{2}$ h) vacuum pumping the SiPM dark rate stabilizes at the same level as in air STP.[9]

Three types of measurements were performed under different conditions of light illumination and wavelength and SiPM over-voltage: (i) current–voltage (I–V) "static" curves, (ii) pulse counting by threshold crossing and (iii) pulse waveform analysis. The light intensity was properly tuned for limiting below the level of $\sim 3\%$ saturation and gain non-linearity effects, related to the presence of R_q and R_b respectively.

3. Measurements and discussion

3.1. Current–voltage characteristics and breakdown

The forward-bias I–V curves measured at various T are shown in Fig. 1. At low current levels ($I_{fwd} < 1\,\mu$A) the curve is fairly described [2] by the empirical law $I_{fwd} \propto \exp(q_e V / \eta kT)$ and is dominated by the diffusion current ($\eta \sim 1$). The linear V–T dependence in $V = V_0 - (\eta k / q_e) T \ln(I_{fwd} / I_0)$ at fixed current I_{fwd} can be used for the precise measurement of the junction temperature. We exploited this effect for cross-checking the value of T of our devices by injecting a constant current of 100 nA and measuring the voltage drop V. At higher current levels the dependence on V_{bias} becomes linear due to the voltage drop on the series resistances, consisting in the parallel of the cells' quenching resistance (R_q / N_{cell}), in the silicon neutral region resistance R_n and in the external resistor R_b. From a linear fit of the curves at high current we extract the values of R_q, ranging from 0.48 MΩ at T_{room} up to ~ 90 MΩ at $T = 50$ K. R_q is empirically parametrized as $R_q(T) \sim 0.13[1 + (300\,\text{K}/T) \exp(300\,\text{K}/T)]$ MΩ.

We measured the reverse-bias I–V curves in the range $50\,\text{K} < T < 320\,\text{K}$. The shape of the curves agrees with the measurements at T_{room} discussed in Ref. [1]: up to the breakdown voltage (V_b) the reverse current increases linearly due to surface leakage; above V_b the breakdown current onsets with quadratic dependence on the over-voltage. We extracted V_b from the curves

[5] PicoQuant laser (driver model PDL-200), pulse width ~ 40 ps FWHM.

[6] Keitley model 2410, current resolution ~ 2 pA.

[7] CPTA model 611, with custom input stage ($Z_{in} = 50\,\Omega$), gain $\times 30$, band-width ~ 350 MHz.

[8] LeCroy model WaveRunner-104Xi, 2 GHz analog bandwidth, sampling at 20 GS/s.

[9] Moderate backing at 50 °C, allows to speed up dark rate stabilization. Before biasing the SiPM the pressure in the vacuum chamber must be reduced below 10^{-1} mbar to prevent discharges.
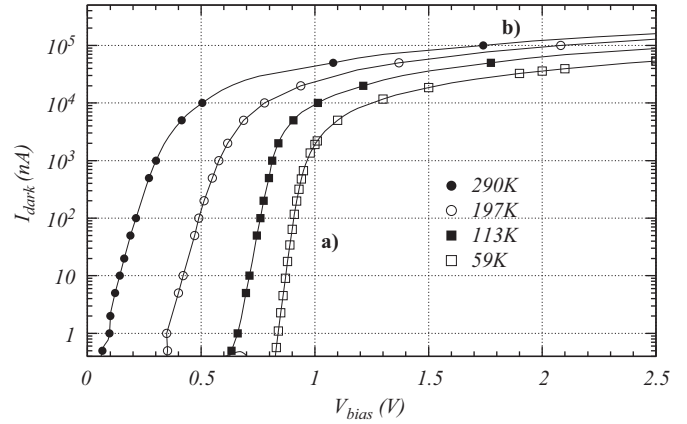
Fig. 1. I–V forward characteristics at various temperatures. Low current region: (a) the voltage drop depends linearly on T. High current region: (b) the current is limited by the series resistance. Lines are drawn as eye guide.
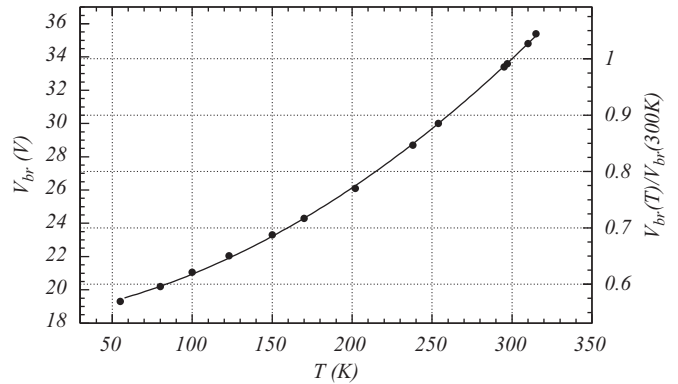

Fig. 2. Breakdown voltage as a function of temperature. The measured values are compatible with the calculations of V_b / V_b (300 K) in silicon abrupt junctions [4]. The line is drawn as eye guide.

according to the parabolic fit procedure discussed in Ref. [1]. Fig. 2 shows the dependence of V_b as a function of T. V_b decreases with T as expected, due to the increase of ionization rates at low T [2,3]. The smooth dependence is compatible with the calculations of V_b / V_b (300 K) in Ref. [4] for abrupt junctions with doping at the level of $\sim 5 \times 10^{13}$ cm^{-3}.

3.2. Signal shape, recovery time and gain

The signal formation in SiPM is understood in terms of equivalent-circuit as discussed in Ref. [5]. The single cell behaviour is modeled by the parallel connection of the detector capacitance (C_d) and the resistance of the micro-plasma (R_d), in series with the parallel connection of the quenching resistance (R_q) and its associated stray capacitance (C_q). The whole SiPM device is described by the parallel connection of N_{cell} cells and the capacitance of the conducting grid for distributing the bias potential. The signal results in a linear combination of two pulses ("slow" and "fast") with a sharp common rising edge, with time constant $\tau_{rise} \sim R_d(C_q + C_d)$, and exponentially falling "slow" and "fast" edges with time constants $\tau_{slow} \sim R_q(C_q + C_d)$ and $\tau_{fast} \sim C_{tot} R_{in}$ respectively. The former "slow" pulse is related to the charge recovery of the single cell. We analyzed the signal waveform and confirmed the model in Ref. [5] by measuring the

two components, which at low T are clearly separated, due to the strong dependence of R_q on T.

We measured the gain G of our samples by illuminating them at low intensity, integrating the current pulses and by fitting the typical comb shaped charge spectrum related to 1photo-electron, 2p.e., 3p.e., etc. We found that the linear slope of G as a function of the over-voltage ΔV is not affected by T. This is because G is related to the charge stored in the cells ($G = (C_d + C_q)\Delta V/q_e$) whose capacity is independent of T.

3.3. Dark noise

The dark count rate (DCR) is measured by counting single carrier generated pulses at fixed ΔV as a function of T. The DCR curve (Fig. 3) shows a steep descent which is fairly proportional to $T^{1.5}\exp E_g/kT$ with an activation energy of $E_g \sim 0.36\,\text{eV}$. In the range $200\,\text{K} < T < 300\,\text{K}$ the main source of DCR is expected to be Shockley–Read–Hall (SRH) generation enhanced to some extent by trap-assisted tunneling [6] in the high electric field region. Below $\sim 200\,\text{K}$ DCR is dominated by band-to-band tunneling [7], which has a weaker dependence on T. Both the band-to-band tunneling and the enhancement of SRH generation due to trap-assisted tunneling are under investigation by the analysis of DCR as a function of ΔV for different temperature ranges. Below $\sim 150\,\text{K}$ the additional suppression of DCR is not yet well understood. A possible explanation could be related to the onset of carrier freeze-out [3], i.e. additional carrier losses at very low T due to ionized impurities acting as shallow traps.

3.4. Afterpulsing and crosstalk

The afterpulsing probability (P_{ap}) is measured by means of waveform analysis: we trigger on single carrier generated pulses and count the subsequent pulses (n_{ap}) in a fixed time interval (5 μs). In order to exclude afterpulses from preceding avalanches, we trigger only on pulses with no previous pulses within an interval of 5 μs. After subtracting the contribution from DCR we extract $P_{ap} = n_{ap}/(1+n_{ap})$, where we take into account afterpulsing cascades. P_{ap} is shown in Fig. 4 as a function of T at fixed $\Delta V = 2\,\text{V}$ and as a function of ΔV at various T. P_{ap} is almost constant and
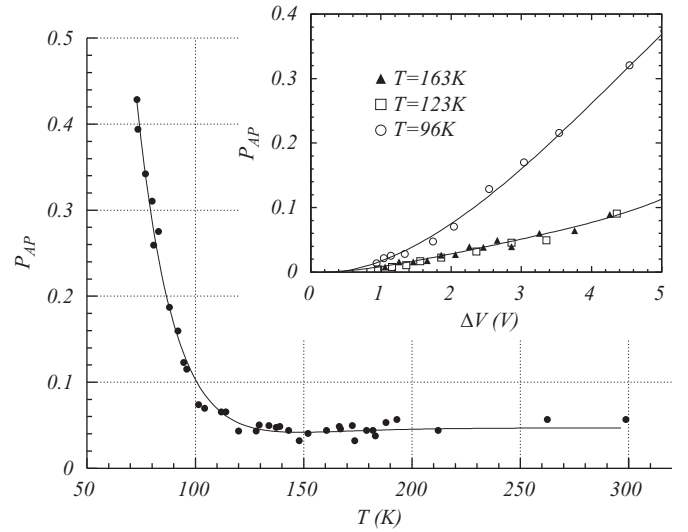
Fig. 4. Afterpulsing probability (P_{AP}) as a function of T at $\Delta V = 2\,\text{V}$. The inset depicts P_{AP} as a function of ΔV. Lines are drawn as eye guide.

compatible with the measurements at T_{room} in Ref. [1], down to $\sim 110\,\text{K}$ where it starts rising swiftly as T is further decreased.

Afterpulsing is related to carrier trapping, during avalanches, and subsequent delayed release generating additional avalanches. Studies are ongoing for characterizing the various traps by analyzing their lifetime evolution as a function of T. A possible explanation for the behaviour below $\sim 110\,\text{K}$ is that new traps become active, which are related to carrier freeze-out.

The crosstalk probability (P_{ct}) is measured by means of the analysis of the dark pulses waveform. We find P_{ct} at a level compatible with that measured in Ref. [1] and we do not observe any dependence of crosstalk on T. This is not fully understood since P_{ct} is proportional [1] to gain and to avalanche triggering probability (P_{trigg}): the former is independent of T in contrast with the latter that might vary with T, as we mention in Section 3.5.

3.5. Photo-detection efficiency

Photo-detection efficiency (PDE) is measured both with pulsed and continuous light (CW) at low intensity: in pulsed mode we take the ratio (PDE′) between the number of single carriers counted in coincidence with the laser trigger and the number of photons measured by the calibrated photo-diode. In CW mode we take the ratio between the current drawn by the SiPM, divided by the measured SiPM gain, and the number of photons measured by the calibrated photo-diode. In both cases the measured ratio PDE′ differs from the absolute PDE by a constant factor, which represents the ratio between the photon acceptance of the SiPM and the photon acceptance of the calibrated photo-diode. We regularly checked that this geometrical factor did not change during the measurements, in order to ensure that PDE′ coincide with the absolute PDE but for an arbitrary constant factor common to all measurements.

Fig. 5 (main box) shows the PDE measured with the halogen lamp as a function of T at $\Delta V = 2\,\text{V}$ and for $\lambda = 300, 500, 800\,\text{nm}$. Each data set at a given λ is normalized to its own PDE value at $T = 297\,\text{K}$. We notice that the shape of this curve is similar when PDE is measured in pulsed mode.

The PDE is the product of three factors: fraction of active area (fill factor), efficiency for photo-conversion, and avalanche triggering probability (P_{trigg}). We expect that, as temperature decreases, different phenomena affect PDE: (i) the attenuation
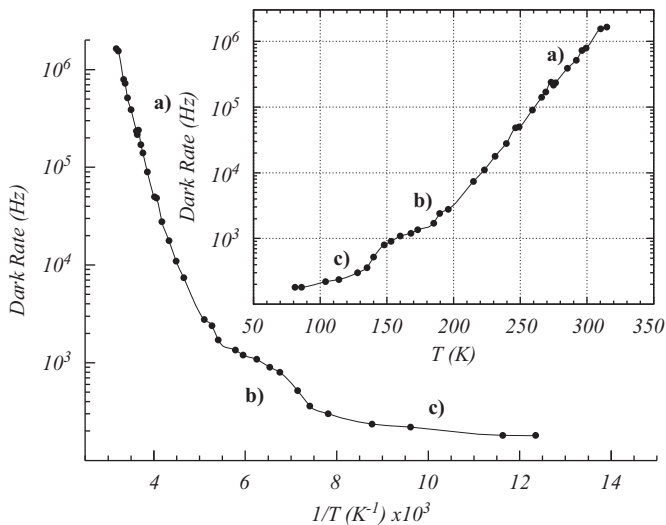
Fig. 3. Dark counting rate (DCR) as a function of T at $\Delta V = 1.5\,\text{V}$: Arrhenius plot and linear plot (inset). DCR sources are indicated: (a) SRH generation (enhanced by trap-assisted tunneling), (b) band-to-band tunneling, (c) additional mechanism (under investigation). Lines are drawn as eye guide.
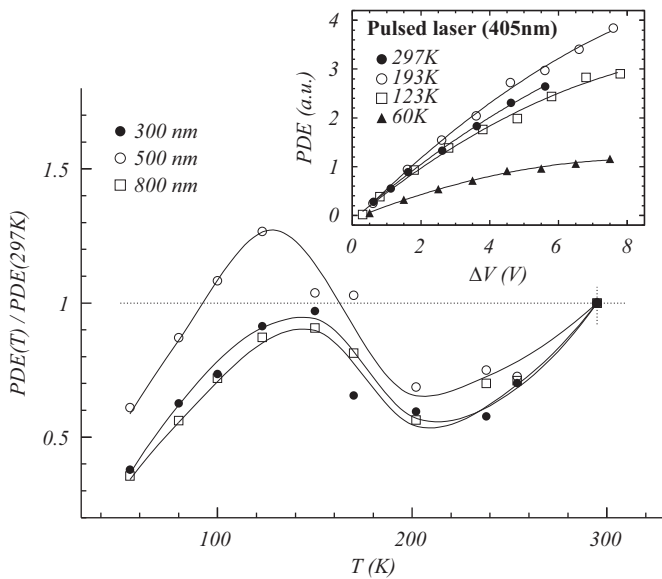
Fig. 5. Photo-detection efficiency (PDE) as a function of T at $\Delta V = 2$ V. Each data set at fixed λ is normalized to the value at $T = 297$ K. The inset depicts the PDE as a function of ΔV. Lines are drawn as eye guide.
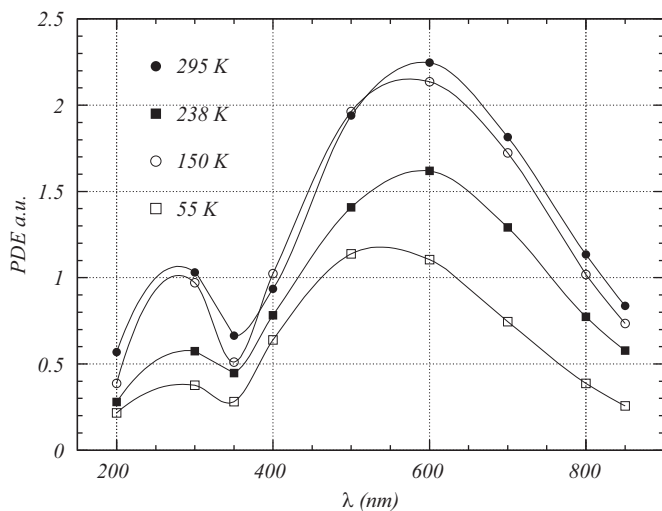

Fig. 6. PDE as a function of λ at $\Delta V = 2$ V. The measured PDE coincides with the absolute PDE but for an arbitrary constant factor common to all measurements. Lines are drawn as eye guide.

length for photo-conversion increases at lower temperatures due to wider energy gap, thus reducing PDE especially for longer wavelengths; (ii) P_{trigg} increases due to the enhanced mobility, thus PDE is increasing at all wavelengths; (iii) onset of carrier freeze-out below ~ 120 K resulting in additional carrier losses. The latter effect could explain the drop of PDE below 120 K, while an interplay between the two former effects could explain the

PDE modulation at higher temperatures. PDE enhancement at low T is observed also in SPAD devices [8]; the drop of efficiency between 300 and 200 K is measured also in APD devices [9,10]. The PDE evolution with temperature can be observed also in Fig. 6 which shows the PDE dependence on λ at $\Delta V = 2$ V and for some values of T. The shape of PDE as a function of λ at T_{room} is fairly compatible above 350 nm with the measurements in Ref. [11].

The analysis of the PDE dependence on T and on λ deserves further investigation for a more quantitative interpretation. The first step of this ongoing work is the study of the basic equations describing P_{trigg} as a function of over-voltage ΔV. For this purpose, we measured the PDE dependence on ΔV in pulsed mode. This is shown in the inset of Fig. 5, where we observe a saturation effect of the PDE at any temperature.

4. Conclusions

We measured the basic properties of SiPMs at low temperatures. The main features we observe are the following: (i) a huge reduction of the dark noise rate by orders of magnitude as T decreases, (ii) a sudden increase of the afterpulsing probability below 100 K and (iii) a modulation, up to $\pm 50\%$ with respect to T_{room}, of the photon detection efficiency, which is in general decreasing at low T, except in the region between ~ 200 and ~ 100 K. Further data analysis and studies of the physics phenomena involved are ongoing. We conclude that SiPMs reach the state of the art sensitivity in light detection at low temperatures and represent an excellent alternative to PMTs, particularly in the range 100 K $< T < 200$ K.

References

[1] C. Piemonte, et al., IEEE Trans. Nucl. Sci. NS-54 (2007) 236.
[2] K.K. Ng, S.M. Sze, Physics of Semiconductor Devices, Wiley, 2006.
[3] M.J. Dean, et al., Low Temperature Electronics, Academic Press, 2001.
[4] C.R. Crowell, S.M. Sze, Appl. Phys. Lett. 9 (1966) 242.
[5] F. Corsi, et al., Nucl. Instr. and Meth. A 572 (2007) 416.
[6] G.A.M. Hurkx, et al., IEEE Trans. Electron Devices ED-39 (1992) 2090.
[7] R.H. Haitz, J. Appl. Phys. 36 (1965) 3123.
[8] I. Rech, et al., Rev. Sci. Instr. 78 (2007) 063105.
[9] L. Yang, et al., Nucl. Instr. and Meth. 508 (2003) 388.
[10] E.B. Johnson, et al., in: Proceedings of the IEEE Nuclear Science Symposium, 2009, p. 2108.
[11] C. Piemonte, et al., in: Proceedings of the IEEE Nuclear Science Symposium, 2006, p. 1566.